



Aerodynamic and structural characteristics of helicopter rotor in circling flight



Xu ZHOU, Xiayang ZHANG, Bo WANG, Qijun ZHAO *

National Key Laboratory of Helicopter Aeromechanics, Nanjing University of Aeronautics and Astronautics, Nanjing 210016, China

Received 11 November 2022; revised 29 January 2023; accepted 2 April 2023
Available online 29 July 2023

KEYWORDS

Aerodynamic load;
Circling state;
Free wake method;
Modal superposition
method;
Structural load

Abstract To investigate the distinct properties of the helicopter rotors during circling flight, the aerodynamic and dynamic models for the main rotor are established considering the trim conditions and the flight parameters of helicopters. The free wake method is introduced to compute the unsteady aerodynamic loads of the rotor characterized by distortions of rotor wakes, and the modal superposition method is used to predict the overall structural loads of the rotor. The effectiveness of the aerodynamic and the structural methods is verified by comparison with the experimental results, whereby the influences of circling direction, radius, and velocity are evaluated in both aerodynamic and dynamic aspects. The results demonstrate that the circling condition makes a great difference to the performance of rotor vortex, as well as the unsteady aerodynamic loads. With the decrease of the circling radius or the increment of the circling velocity, the thrust of the main rotor increases apparently to balance the inertial force. Meanwhile, the harmonics of aerodynamic loads in rotor disc change severely and an evident aerodynamic load shock appears at high-order components, which further causes a shift-of-peak-phase bending moment in the flap dimension. Moreover, the advancing side of blade experiences second blade/vortex interaction, whose intensity has a distinct enhancement as the circling radius decreases with the motion of vortices.

© 2023 Production and hosting by Elsevier Ltd. on behalf of Chinese Society of Aeronautics and Astronautics. This is an open access article under the CC BY-NC-ND license (<http://creativecommons.org/licenses/by-nc-nd/4.0/>).

1. Introduction

Helicopters rely on fuselage roll and tail rotor manipulation to realize coordinated turn to accommodate complex terrain,

which occupies a large proportion of flight spectrums.¹ Since the aerodynamic load and aero-elastic effects of rotor blades are greatly different from those in steady flight, it is necessary to study the impacts of potential physical phenomena caused by different flight parameters on the aerodynamic and structural loads of the rotor in circling.

Blades produce distorted tip vortices during the maneuvering flight, which enhance the complexity of aerodynamic loads analysis. To address such a problem, Yang and Aoyama² proposed a hybrid method by dividing the maneuvering motion of helicopters into translation and rotation, and then captured the tip vortex in two cases (accelerating/decelerating flight

* Corresponding author.

E-mail address: zhaoqijun@nauu.edu.cn (Q. ZHAO).

Peer review under responsibility of Editorial Committee of CJA.



Production and hosting by Elsevier

and right-turn flight, as shown in Fig. 1) after a new governing equation is derived based on the Computational Fluid Dynamics (CFD) method. Braukmann et al.³ found by means of experiment that the collective and cyclic pitch variations are the main influence on the vortex structure. Huang and Peters⁴ actualized the real-time simulation of potential flow based on a nonlinear states-space model of the induced flow.

The dynamic characteristics analysis and vibration load estimation are important parts of rotor performance analysis.^{5–6} Ferhatoglu et al.⁷ used different modal shapes to carry out nonlinear vibration analysis according to the modal superposition method. Ma et al.⁸ proposed a Bound Correction Interval Analysis Method (BCIM) based on Chebyshev expansion and modal superposition to overcome the uncertainty of rotor system. Ickes et al.⁹ computed the aerodynamic and structural loads of UH-60A and Bell-427 by coupling the CFD method with the Computational Structural Dynamics (CSD) method. You et al.¹⁰ predicted the rotor aeromechanics by coupling CAMRAD II and KFLOW¹¹ code loosely that the sophisticated structure property of blades was considered. Ma et al.¹² studied the structural characteristics of composite rotors using a novel finite volume method. Zhang et al.¹³ researched the dynamic properties of the two-segment deployable beam by establishing a Lagrange-form governing equation, and explored the regularity of self-adaption beam structures in use.

Nowadays, CFD has significant advantages in simulating details of the flowfield, and the effect of elastic blades can be considered by the CFD/CSD coupling method.^{14–16} Nevertheless, the CFD code relies on a non-inertial coordinate for moving according to the parameters of maneuvering. In addition, the CFD/CSD coupling method is limited by the distribution of three-dimensional pressure on the blade and the accuracy of structural model. The aerodynamic load has a strong periodicity and is the superposition of each harmonic term at different frequencies. On account of the little amplitudes of aerodynamic load at high harmonic numbers, the response under low-order excitation is considered when solving the flapping motion. For the sake of the whole aircraft trimming and the calculation of aerodynamic load, the free wake method^{17–18} is used, wherein the wake is constrained due to circling motion. The modal superposition method^{19–22} can transform the blade to a model with finite degrees of freedom, and is thus adopted to carry out the approximate analytical solution of the blade

response. The variation laws and the mechanism of aerodynamic and structural loads at different harmonic numbers due to potential phenomenon in circling flight are provided by the results of this study, which are beneficial to route planning and flight strategy study.

2. Modeling and solution methodologies

2.1. Aerodynamic model

The rotor vortex sheds from the blade trailing edge and tip continuously, and evolves into a helical system. As the main form of the flowfield, it interacts with the blade, tail rotor and fuselage, and thereby changes the rotor aerodynamic load. The continuous vortex space is substituted by the linear vortex segments using the free wake method. The flowfield outside the vortex tube is described by the vorticity equation of incompressible viscous flow as follows:

$$\frac{\partial \boldsymbol{\omega}}{\partial t} = -\mathbf{u} \cdot \nabla \boldsymbol{\omega} + \boldsymbol{\omega} \cdot \nabla \mathbf{u} + v \Delta \boldsymbol{\omega} \quad (1)$$

where $\boldsymbol{\omega}$ is the vorticity defined by $\boldsymbol{\omega} = \nabla \times \mathbf{u}$, \mathbf{u} is the flow velocity, and v is the coefficient of kinematic viscosity.

The induced velocity of the flowfield is calculated by Biot-Savart's law, and the velocity at each point can be derived by the following equation:

$$\begin{aligned} \mathbf{u} &= \mathbf{u}_\infty - \mathbf{u}_{in} \\ &= \mathbf{u}_\infty - \frac{1}{4\pi} \int_V \frac{\boldsymbol{\omega}(x_0) \times (x_0 - \mathbf{x})}{|x_0 - \mathbf{x}|^3} dV \end{aligned} \quad (2)$$

in which x_0 presents the position of each vortex segment, \mathbf{x} is the position where velocity needs to be calculated, and V represents the whole flowfield.

The control points are uniformly set at $0.75c$ (c is the length of chordline) on the blade surface and determine the regenerated position of vortices. The intensity of a newly-formed vortex is calculated according to the conservation of circulation, i.e.,

$$\gamma_\omega = -\frac{d\Gamma_b}{dt} + v_b \nabla \cdot \Gamma_b \quad (3)$$

where γ_ω represents the circulation of a new-formed vortex, v_b represents the relative velocity of air, and Γ_b represents the circulation of blade section.

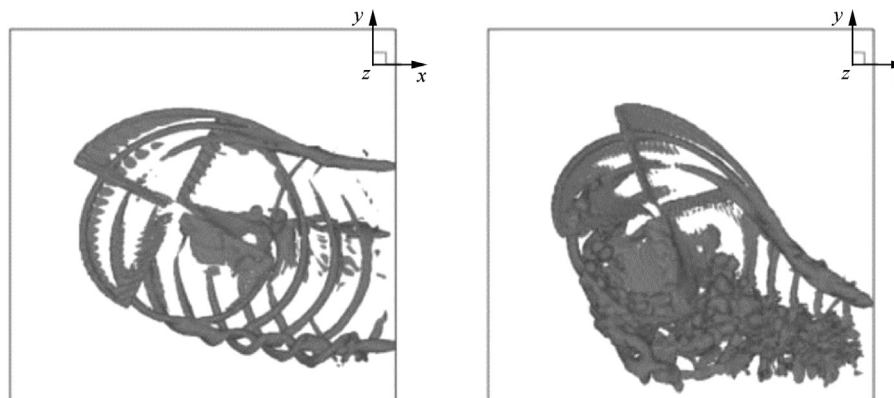


Fig. 1 Top view of typical iso-surface of vorticity for right-turn flight.²

The second-order time marching scheme is introduced to conduct the vortex simulation, which is

$$\mathbf{x}^{n+1} = \mathbf{x}^n + \frac{\Delta t}{2} (3\mathbf{u}^n - \mathbf{u}^{n-1}) \quad (4)$$

in which \mathbf{x}^n and \mathbf{u}^n represent the coordinate of the origin point and the velocity of the end point of each vortex segment at the n th time step, respectively.

Considering the distortion of the free wake, the core model and the lifetime model of the vortex are introduced as follows:

$$v_\theta(r) = \frac{\Gamma r}{2\pi(r_c^{2n} + r^{2n})^{1/n}} \quad (5)$$

$$r_c = 2.242 \sqrt{\delta v \left(\frac{\zeta - \zeta_0}{\Omega} \right)} \quad (6)$$

where v_θ is the tangential velocity distribution along the radius of vortex, and here $n = 2$ is utilized; r_c is the radius of vortex core and is affected by the lifetime ζ ; δ and v represent the perturbation viscosity coefficient and the kinematic viscosity coefficient, respectively.

The Beddoes model²³ that is capable of considering the compressibility and stall characteristics of the airfoil is utilized to compute the unsteady aerodynamic load. The normal force coefficient is expressed as

$$C_n = \frac{2\pi}{\sqrt{1-Ma^2}} \left(\frac{1+\sqrt{f}}{2} \right)^2 \alpha \quad (7)$$

where Ma , f and α are the Mach number, the flow separation position and the actual angle of attack of each blade section, respectively. Herein, f can be obtained by the following judgements

$$f = \begin{cases} 1 - 0.3 \exp \left[\frac{(\alpha - \alpha_0) - \alpha_1}{S_1} \right], & \alpha < \alpha_1 \\ 0.04 + 0.66 \exp \left[\frac{\alpha_1 - (\alpha - \alpha_0)}{S_2} \right], & \alpha > \alpha_1 \end{cases} \quad (8)$$

where α_0 is the zero-lift angle, and α_1 is the stall angle when $f = 0.7$; S_1 and S_2 are the static-stall related factors which

are influenced by the Mach number. The lift and drag coefficients can be eventually expressed as

$$C_L(\alpha) = C_n \cos \alpha - C_d \sin \alpha \approx \frac{2\pi}{\sqrt{1-Ma^2}} \left(\frac{1+\sqrt{f}}{2} \right)^2 \alpha \cos \alpha \quad (9)$$

$$C_D = C_{D_0} + 0.035 C_n \sin \alpha + K_d C_n \sin(\alpha - \alpha_{DD}) \quad (10)$$

in which

$$K_d = \begin{cases} 0, & \alpha < \alpha_{DD} \\ 2.7 \exp(-d_f), & \alpha > \alpha_{DD} \end{cases} \quad (11)$$

$$d_f = 6.1 - 7Ma + 0.5 \exp \left[- \left(\frac{Ma - 0.65}{0.125} \right)^2 \right] \quad (12)$$

where C_{D_0} is the drag coefficient at the zero-lift state, and α_{DD} is the drag divergence angle.

2.2. Wake correction during circling flights

Fig. 2 depicts the coordinate systems for the aerodynamic analysis of helicopter during circling motion, in which $O_f x_f y_f z_f$ is the fuselage coordinate system which sits at the gravity center of helicopter, $O_g x_g y_g z_g$ denotes the ground coordinate system, and $O_R x_R y_R z_R$ is the ground rotation coordinate system located at the circling center. Herein, θ, γ and α_s are the pitch angle, roll angle and the tilt angle of rotor axis, respectively.

In the actual simulations, the initial rigid wake is determined by the direction, radius, and velocity of the circling flight, and is converted downstream the flowfield. **Fig. 3** shows the comparison of the initial rigid wakes between the level flight and the circling flight from the top view of the rotor. Here, $Oxyz$ is the rotor hub coordinate system, $Ox'y'z'$ is a coordinate system set at the center of last-circle wake, R_{cir} is the circling radius, and α_c is the central angle of the wake. The plot shows that in addition to the backward movement, there is also apparent lateral movement of the wake.

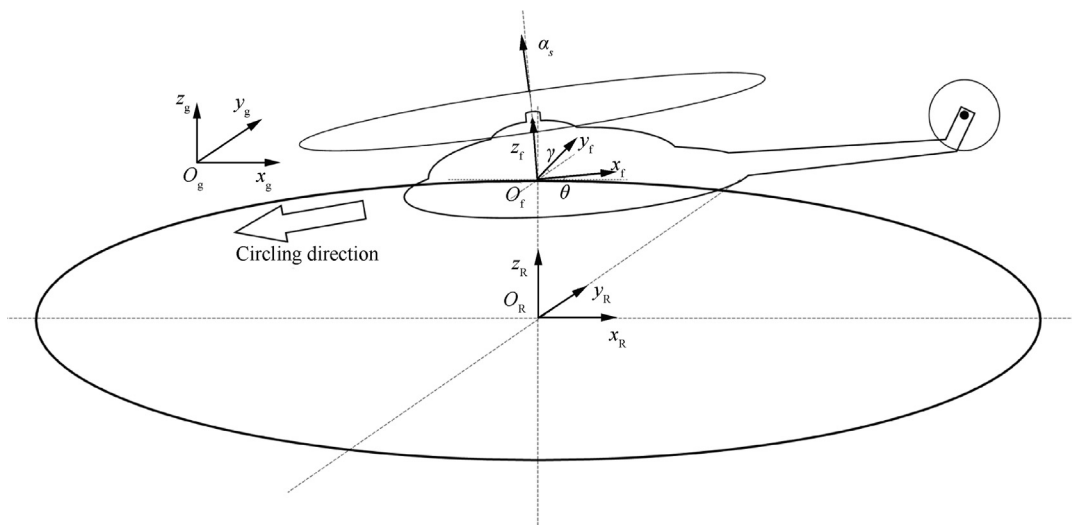


Fig. 2 Coordinate systems of helicopter during circling motion.

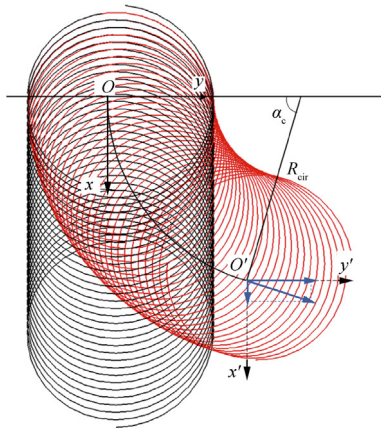


Fig. 3 Rigid wake when the helicopter rotor performs a circling task.

When initializing the rigid wake model, the difference of position constraint of the vortex due to circling motion is imposed in the rotor coordinate system, which is shown in Eq. (13).

$$\Delta \mathbf{X} = \begin{bmatrix} \Delta x \\ \Delta y \\ \Delta z \end{bmatrix} = \begin{bmatrix} R_{\text{cir}} \sin \alpha_c - \alpha_c R_{\text{cir}} \\ R_{\text{cir}} - R_{\text{cir}} \cos \alpha_c \\ 0 \end{bmatrix} \quad (13)$$

where $(\Delta x, \Delta y, \Delta z)$ is the additional position constraint of the vortex relative to the level flight.

The steady-motion result is applied to the vortex segments at first in the simulation of wake motion. Note that the large roll angle γ in the circling state is a crucial factor. According to Fig. 3, the additional velocity constraint expressed as the following equation is imposed to the vortex in $Oxyz$.

$$\Delta \mathbf{V} = \begin{bmatrix} \Delta u \\ \Delta v \\ \Delta w \end{bmatrix} = \begin{bmatrix} \mu \Omega R \sin \alpha_c \\ \mu \Omega R \cos \alpha_c \sin \gamma \\ \mu \Omega R \cos \alpha_c \cos \gamma \end{bmatrix} \quad (14)$$

where μ is the advance ratio, Ω is the rotation velocity of the rotor, R is the radius of the rotor, and $(\Delta u, \Delta v, \Delta w)$ is the additional velocity constraint of the vortex relative to the rotor.

2.3. Trim method

The helicopter during circling motion is trimmed to compute the actual aerodynamic and structural loads of the rotor. The trim targets are composed of the forces and moments along the direction indicated by the subscript, i.e., the vector $\mathbf{Y} = [F_x \ F_y \ F_z \ M_x \ M_y \ M_z]$; the input variables are the collective and cyclic pitches of the main rotor, the collective pitch of the tail rotor and the attitude angle of the helicopter, i.e., $\mathbf{X} = [\theta_c \ \theta_e \ \theta_a \ \theta_r \ \theta \ \gamma]$. The helicopter can achieve self-balance in the yaw motion, and the heading angle also changes with the circling flight harmoniously. Besides, the force and moment coefficients of the fuselage can be obtained from the experimental data or the databases, and the aerodynamic loads of the tail rotor are calculated by the blade element theory. Further, the Newton iterative method, as shown in Eq. (15), is used in the trim process.

$$\mathbf{X}^{n+1} = \mathbf{X}^n - \mathbf{J}^{-1} F(\mathbf{X}^n) \quad (15)$$

in which \mathbf{X}^i is the input variables of the i -th step, $F(\mathbf{X}^i)$ is the state variable, and \mathbf{J} is the Jacobian matrix derived by the differential item as follows:

$$\mathbf{J}_{ij} = \frac{\partial Y_i}{\partial X_j} = \frac{\Delta Y_i}{\Delta X_j} \quad (16)$$

In Eq. (17), F_y is further modified in the ground rotation coordinate system.

$$F_y = m_1 (\mu \Omega R)^2 / R_{\text{cir}} \quad (17)$$

where m_1 is the mass of the helicopter.

2.4. Solution for blade motion

The equilibrium equation in the flap dimension is derived according to the elemental force analysis shown in Fig. 4.

The forces within each blade segment include the shear force Q , the bending moment M , the centrifugal force T and the distribution load f_d on the blade (f_d consists of the aerodynamic load f_{aero} and the internal force; e is the offset of the flap hinge). The equilibrium equation is established as follows:

$$\begin{cases} \frac{\partial Q}{\partial x} + f_d = 0 \\ (EI_y \ddot{y}'')'' - (Ty')' + m\ddot{y} = f_{\text{aero}} \end{cases} \quad (18)$$

in which EI_y and m are the stiffness and mass of the blade segment, respectively.

The mode superposition method is introduced to express the solution for flapping motion.

$$y(x, t) = \sum_{i=1}^n \gamma_i(x) q_i(t) \quad (19)$$

where $\gamma_i(x)$ is the i -th modal shape of the blades, and $q_i(t)$ is the corresponding response quantity.

The inherent characteristics are approximated by virtue of the Galerkin method and the general displacement functions \tilde{y} , and the inertial matrix and stiffness matrix are expressed as

$$\begin{cases} \mathbf{M}_{ij} = \int_e^R m \tilde{y}_i \tilde{y}_j dx \\ \mathbf{K}_{ij} = \int_e^R (EI_y \tilde{y}_j'')'' \tilde{y}_i dx - \int_e^R (T \tilde{y}_j')' \tilde{y}_i dx \end{cases} \quad (20)$$

where \tilde{y} should satisfy the boundary conditions of an articulated hub that is considered here without loss of generality.

$$\tilde{y}(e) = 0, EI \tilde{y}''(e) = K \tilde{y}'(e), \tilde{y}''(R) = 0, \tilde{y}'''(R) = 0 \quad (21)$$

According to linear superposition, the modal shapes of the rotor blade can be written as

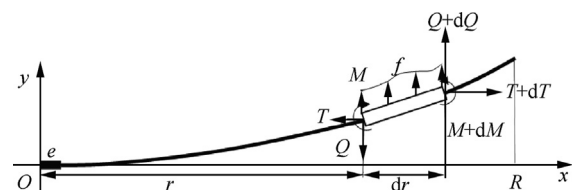


Fig. 4 Diagram of force analysis of blade micro-segment in flapping direction.

$$\mathbf{F}_s(x) = \Phi \tilde{\mathbf{F}}_s(x) \quad (22)$$

where Φ is a matrix of eigenvectors.

The inertial matrix and stiffness matrix can be obtained by applying Eq. (22) to Eq. (20), and the modal force can be calculated by

$$F_i = \int_e^R \gamma_i f_{\text{aero}} dx \quad (23)$$

The periodic aerodynamic loads are written in the Fourier transformations by taking the rotation frequency as reference.

$$f_{\text{aero}}(x, t) = f_0(x) + \sum_i^n [f_{ic}(x) \cos(i\Omega t) + f_{is}(x) \sin(i\Omega t)], \\ i = 1, 2, \dots, n \quad (24)$$

where $f_0(x)$ is the mean load, and $f_{ic}(x)$ and $f_{is}(x)$ are the amplitudes of different harmonic terms. The different harmonics are summed up by virtue of the Fourier transform, in which the stationary one only leads to the steady-state deformation of the blade, and the contributions of the periodic parts can be described by

$$A_i = \frac{F_i}{K_{pi} (1 - \bar{\omega}_i^2)} \quad (25)$$

where K_{pi} is the i -th modal stiffness, and $\bar{\omega}_i = \omega/\omega_i$ is the ratio of aerodynamic load frequencies at each order to natural frequencies. The responses of the blade can be calculated by imposing explicit aerodynamical loads to the dynamical equation.

The bending moment of flap motion at any blade section can be easily acquired by

$$M_b(x, t) = EI_y z''|_x = \sum_{i=1}^n EI_y(x) \gamma_i''(x) q_i(t) \quad (26)$$

The flowchart of the entire algorithm is available and presented in Fig. 5.

3. Example verification

The UH-60A maneuvering flight is used to validate the accuracy of the aerodynamic method with experimental results, in which the rotor model is in accordance with Table 1 and Fig. 6. The outline of UH-60A blades is depicted in Fig. 6, where the red lines are the separation positions of different airfoils, and the dark line represents the distribution of the twist angle when the collective pitch is 0°. Figs. 7–9 depict the distribution of normal force coefficient of level flight (Flight 8534) and UTTAS pull-up maneuver (Flight 11029). The accuracy of modeling and analysis method is validated by Figs. 7–9. The calculated results are found to be in good agreement with the experimental data, which indicates that the established calculation method can be used for subsequent calculation.

Further, the shape functions satisfying the boundary conditions of blades are constructed to calculate the inherent characteristics, and the results are shown in Table 2. It is demonstrated that compared with UMARC (University of Maryland Advanced Rotorcraft Code), the structural model proposed can accurately predict the natural characteristics at different rotation speeds, and is used for subsequent structural analysis. Fig. 10 presents the resonance graph of UH-60A blades using the proposed method and UMARC, showing that the structural characteristics of blades at the operating speed are consistent. ‘ iF ’ means i -th flap frequency in Fig. 10.

4. Influence of circling parameters on structural load

4.1. Transient changing process

A transient maneuvering process from the level flight to the circling flight at $\mu = 0.05$ and $R_{\text{turn}} = 15$ m are simulated, as

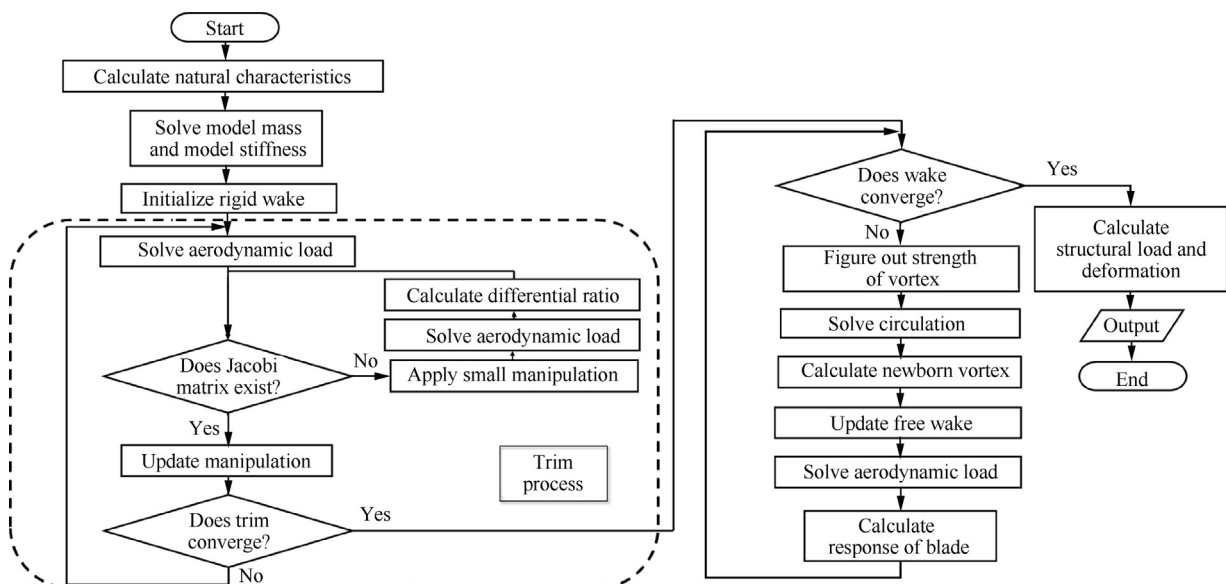
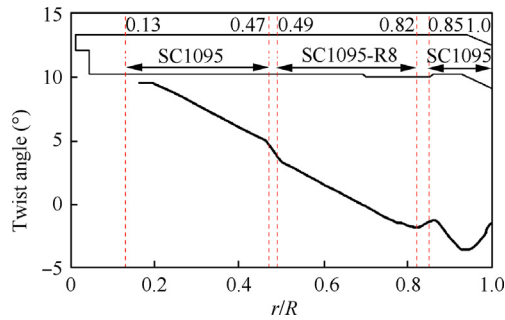
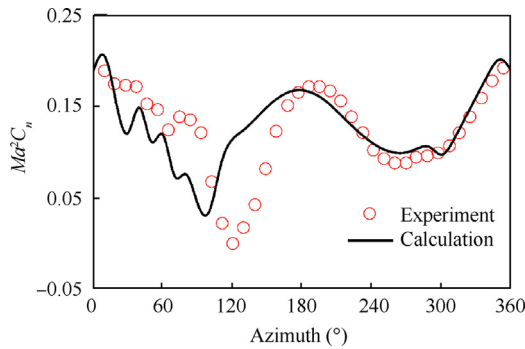


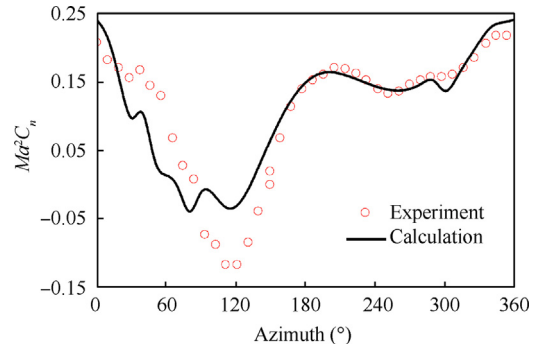
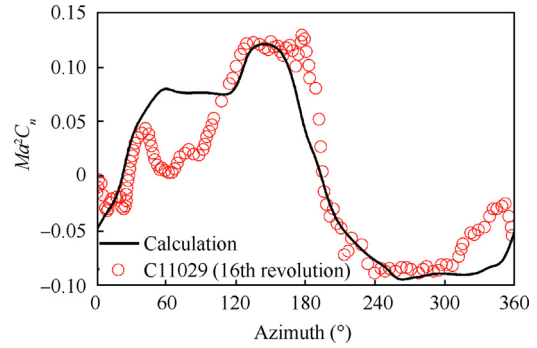
Fig. 5 Solution flowchart of dynamic responses when a helicopter is in circling flight.

Table 1 Parameters of UH-60A main rotor.

Parameter	Value
Numbers of blades	4
Radius(m)	8.178
Chordline length(m)	0.527
Rotating speed(r/min)	258
Offset of flapping hinge(m)	0.381
Backward sweep($^{\circ}$)	20

**Fig. 6** Twist angle and airfoil distribution of UH-60A blades.**Fig. 7** Flight 8534: Normal force coefficient distribution at $r/R = 0.775$.

shown in [Fig. 11](#), and the changing processes include the wake at level flight, transition process and right-turn flight. The end-most vortices in the process from (1) to (2) convert downstream along the local flowfield. However, the newly-formed vortex segments start to accumulate on the inner side of the turn, and thus the blade-vortex interference and the vortex-vortex interference become more apparent compared with those in the level flight. The vortex in the process from (2) to (3) changes into a steady circle, and the influence degree of

**Fig. 8** Flight 8534: Normal force coefficient distribution at $r/R = 0.92$.**Fig. 9** Flight 11029: Normal force coefficient distribution at $r/R = 0.4$.

the vortex that has already existed increases due to the accumulation of wake in the inner side of circling. This process will have great influence on the circumferential distribution of aerodynamic loads.

4.2. Circling direction

[Fig. 12](#) presents the convergent wakes from the top view of the main rotor at ($\mu = 0.04, R_{\text{cir}} = 10$ m) and ($\mu = 0.34, R_{\text{cir}} = 422$ m) conditions, and [Figs. 13 and 14](#) present the aerodynamic results in different directions. Herein, it is selected to show the influence mechanisms around the rotor disc at the spanwise $r/R = 0.7$, and all the computations are trimmed to analyze the evolution of wake and its influence on the aerodynamic and structural loads.

[Fig. 12\(a\)](#) and [Fig. 13\(a\)](#) demonstrate that there are slight differences in aerodynamic loads on account of the distortion of wake influenced by the circling direction. Note that the induced velocity at the rotor disk is changed. In contrast, the

Table 2 Comparison of natural frequencies of UH-60A helicopter blades.

Flap frequency	First order	Second order	Third order	Fourth order
Test value, Ω/Ω_0	1.04	2.87	4.76	7.81
Calculated value, Ω/Ω_0	1.0480	2.8081	4.9592	8.0640
Error(%)	0.7692	-2.1568	4.1849	3.2522

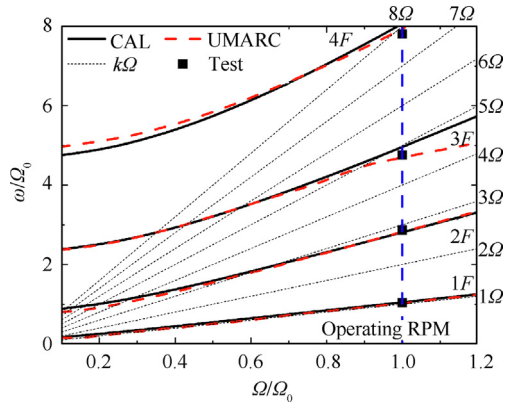


Fig. 10 Resonance graph of UH-60A blades.

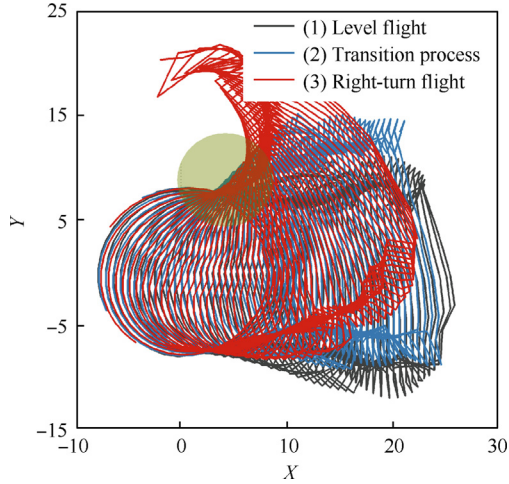
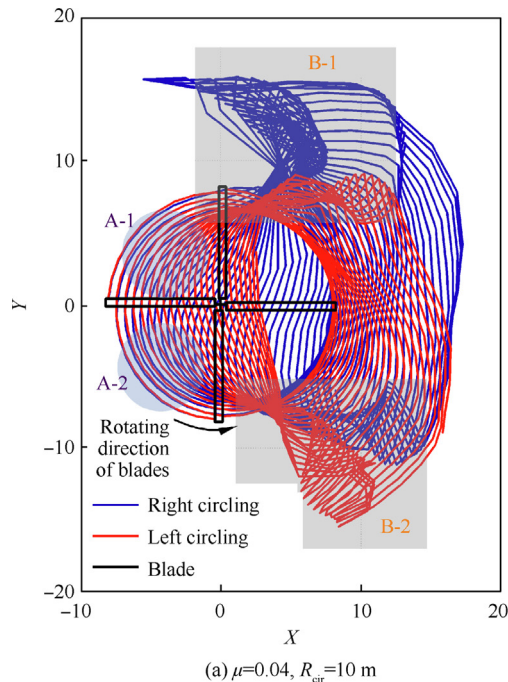


Fig. 11 Top view of free wake shapes for right-turn flight ($\mu = 0.05, R_{\text{turn}} = 15 \text{ m}$).



effect distance between the wake and main rotor, even if the wake is distorted, is relatively far in the case of quick circling as shown in Fig. 12(b). Therefore, the induced velocity in different circling cases has a slight difference, and the aerodynamic loads almost coincide at high flight velocity, as demonstrated in Fig. 14(a). In Fig. 12(a), the motion of wake in Zone A manifests the trend of alienation from the endmost vortices in Zone B and changes the interference distance between the blade and vortices. Therefore, the aerodynamic load oscillates in the inner side of the circling by reason of the blade-vortex interference accompanied by the accumulated vortex in Zone B. Meanwhile, the periodicity of the local area becomes more intense, such as the behavior at the advancing side of the right circling state. In contrast, these phenomena do not appear in Zone C at high flight speed, because the manipulation becomes the dominant factor instead of the induced velocity at this moment. Fig. 12(b) and Fig. 14(b) show the distribution of lateral velocity downwash at $0.5R$, and the results are also consistent with those of the above analysis. The changes of wake position and manipulation affect the aerodynamic loads severely, and result in the change of peak phase in Fig. 13(a) and Fig. 14(a) correspondingly.

Figs. 15 and 16 show the amplitudes of the first four order aerodynamic loads at $\mu = 0.04$ and $R_{\text{cir}} = 10 \text{ m}$ and at $\mu = 0.34$ and $R_{\text{cir}} = 422 \text{ m}$, respectively. In Fig. 15, the first-order term is dominant and the amplitude of high-order aerodynamic load is small and negligible. In different circling directions, the amplitudes of aerodynamic harmonic loads present different variation rules because of the distinct distributions of wakes, e.g., the induced velocity in Fig. 13(b) increases at $\psi = 90^\circ$ when a helicopter circles leftward, and the actual attack angle and aerodynamic loads in Fig. 13(a) are lower when a helicopter circles rightward. This phenomenon enhances the origin harmonic load and the first-order load increases in Fig. 15, which is the dominant component of aerodynamic loads. The difference in circling directions is not obvi-

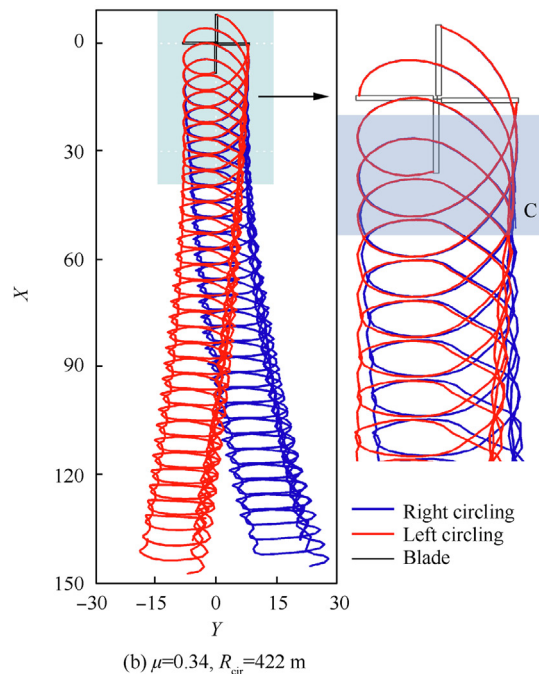


Fig. 12 Vortex distribution in different directions (Top view).

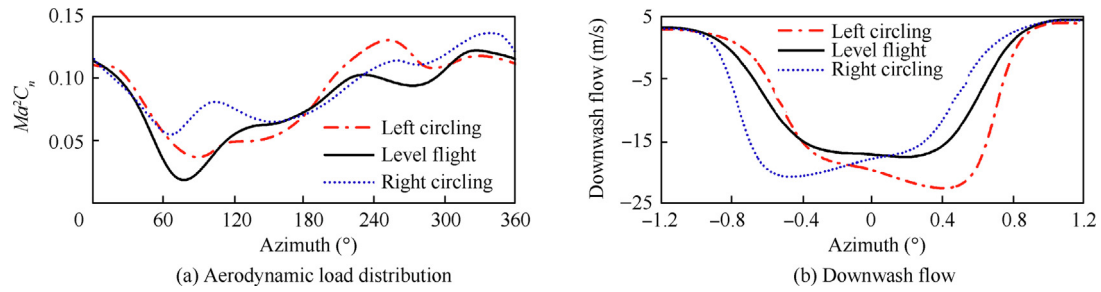


Fig. 13 Results of aerodynamic loads and downwash flow in different directions ($\mu = 0.04, R_{\text{cir}} = 10 \text{ m}$).

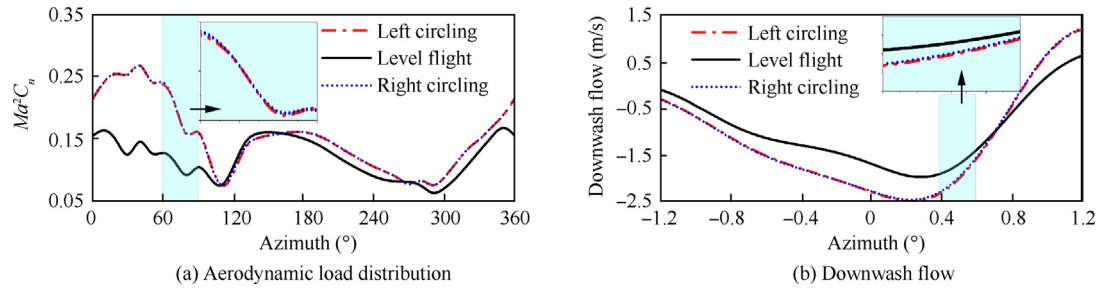


Fig. 14 Results of aerodynamic loads and downwash flow in different directions ($\mu = 0.34, R_{\text{cir}} = 422 \text{ m}$).

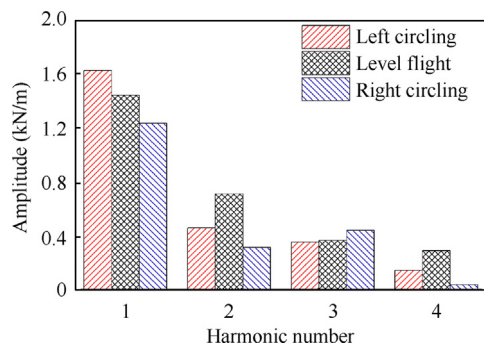


Fig. 15 Amplitude of the first four order aerodynamic load ($\mu = 0.04, R_{\text{cir}} = 10 \text{ m}$).

ous at a high velocity, as shown in Fig. 16, because the manipulation values, induced velocity and pitch angle are similar. Figs. 15 and 16 indicate that the spatial distribution of wake has great influence on aerodynamic loads, and the influence of wake on the inflow is much greater than the change of the

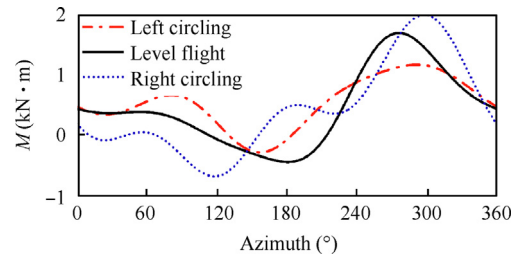


Fig. 17 Circumferential distribution of flap bending moment ($\mu = 0.04, R_{\text{cir}} = 10 \text{ m}$).

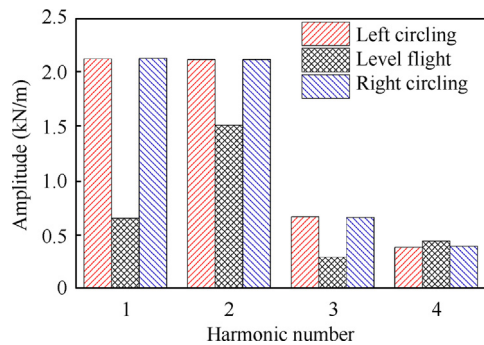


Fig. 16 Amplitude of the first four order aerodynamic load ($\mu = 0.34, R_{\text{cir}} = 422 \text{ m}$).

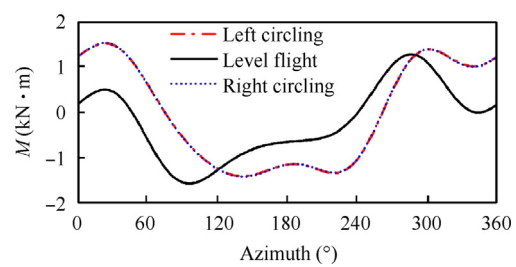


Fig. 18 Circumferential distribution of flap bending moment ($\mu = 0.34, R_{\text{cir}} = 422 \text{ m}$).

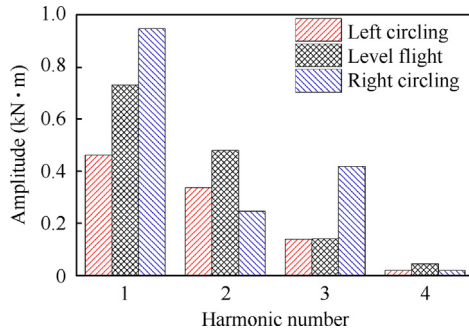


Fig. 19 Amplitude of the first four order structural load ($\mu = 0.04, R_{\text{cir}} = 10 \text{ m}$).

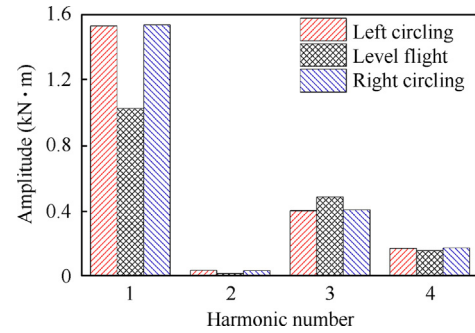
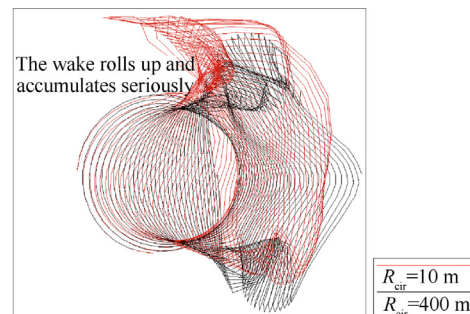
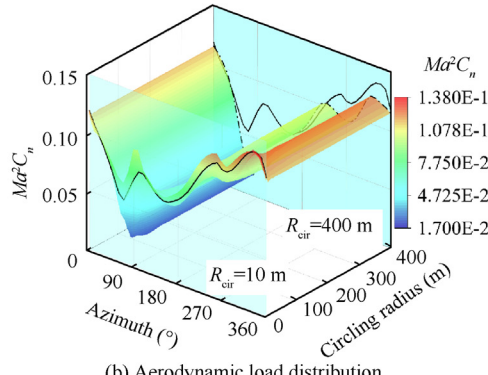


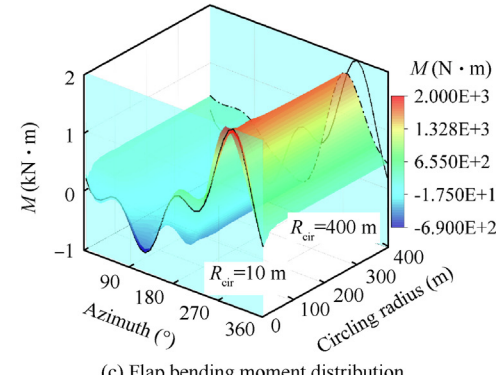
Fig. 20 Amplitude of the first four order structural load ($\mu = 0.34, R_{\text{cir}} = 422 \text{ m}$).



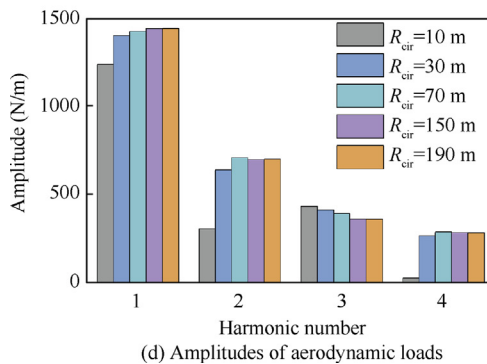
(a) Wake distribution



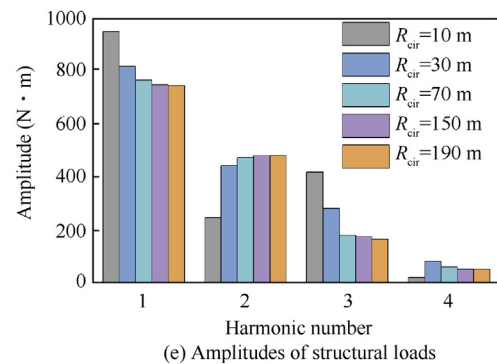
(b) Aerodynamic load distribution



(c) Flap bending moment distribution



(d) Amplitudes of aerodynamic loads



(e) Amplitudes of structural loads

Fig. 21 Wakes, aerodynamic loads, and structural loads around circling radius at $\mu = 0.04$.

induced velocity in the high-velocity circling condition. Note that the aerodynamic load at 4/rev is reduced in both circling directions, which can reduce the structural hub loads transferred to the fuselage.

Figs. 17 and 18 present the circumferential distributions of flap bending moments in different circling directions at different flight conditions ($\mu = 0.04, R_{\text{cir}} = 10 \text{ m}$ and $\mu = 0.34, R_{\text{cir}} = 422 \text{ m}$). Because of the phase hysteresis relationship between the response and the excitation force, the flap bending moments in different circling directions differ from the aerodynamic loads. The flap bending moment at the retreating side decreases in the low-velocity left turn and the advancing side of rotor in the right-turn flight, and the vibration level of rotor falls when the helicopter moves from the level flight to the left-circling. Fig. 18 shows that there is a slight difference between the flap bending moments at high velocity flight, but the flap bending moment is sensitive to the circling direction in low velocity due to the distortion of rotor wake.

Figs. 19 and 20 show the first four order flap bending moments at different conditions ($\mu = 0.04, R_{\text{cir}} = 10 \text{ m}$ and $\mu = 0.34, R_{\text{cir}} = 422 \text{ m}$). Due to the variations in the amplitude and phase of the aerodynamic loads, the flap bending moments

of different harmonics present different changing laws. At low velocity, the bending moments of different order vary with the direction of circling, and the first-order moments exhibit the opposite trend. Nevertheless, the direction of circling does not affect the amplitude of flap moment at high velocity.

4.3. Circling radius and velocity

The circling computation results gradually converge to the level flight with the increment of circling radius, and the rotor thrust increases when the circling radius decreases to balance the circling flight (see Figs. 21 and 22 at $\mu = 0.04$ and $\mu = 0.34$, respectively). In each group of plots, Fig. 21(a) and Fig. 22(a) show the wake distribution at different circling radii, Figs. 21(b)-(c) and Figs. 22(b)-(c) are aerodynamic and structural loads along the azimuth angle, and Figs. 21(d)-(e) and Figs. 22(d)-(e) present the amplitudes of aerodynamic and structural loads in different harmonics with the variation of circling radius.

The aerodynamic loads at low flight velocity are rarely affected by the distortion of the wake when the helicopter approaches the extreme circling radius, where the higher frequencies oscillate obviously. Nevertheless, high-frequency

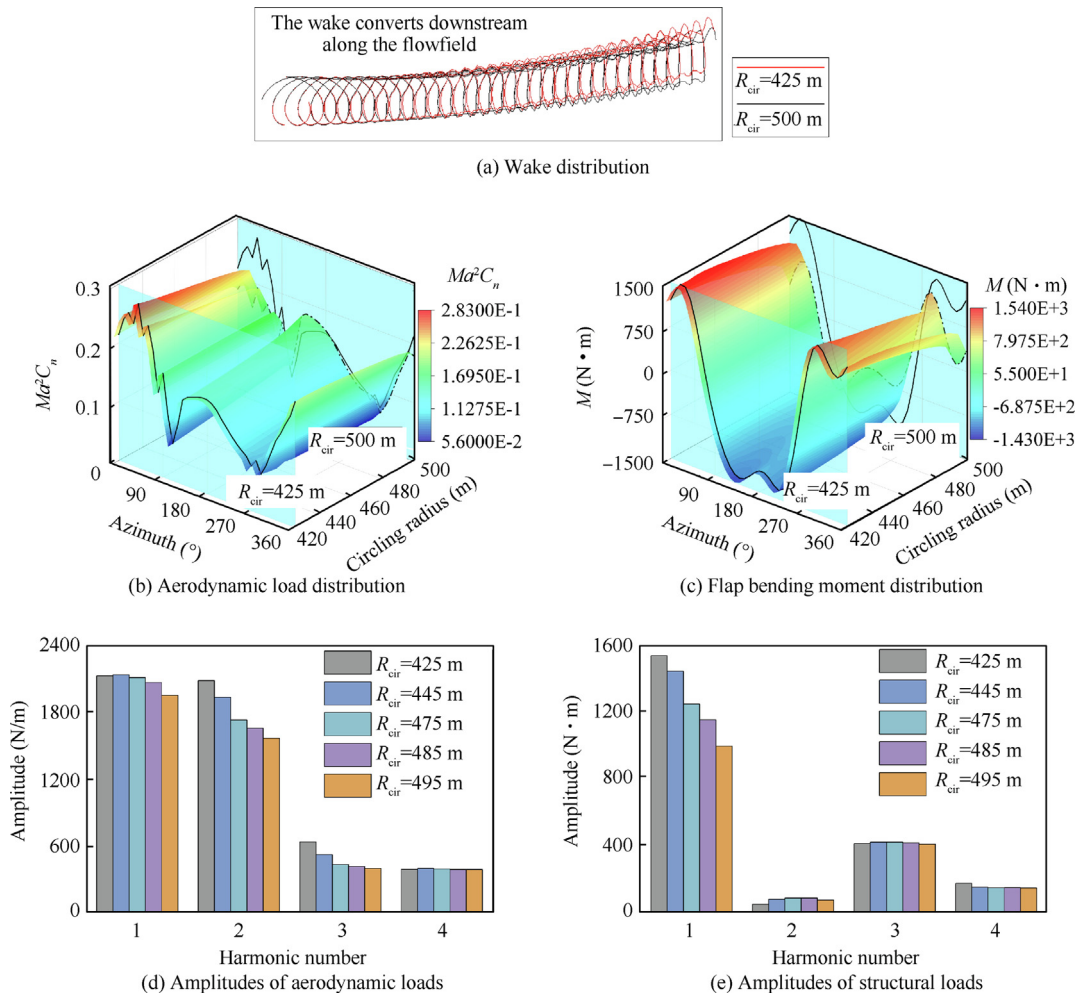


Fig. 22 Wakes, aerodynamic loads, and structural loads around circling radius at $\mu = 0.34$.

oscillation, instead of the shift of peak and valley phase, disappears in the small circling radius at high-velocity circling. The distortion of wake and the value of manipulation have different effects on the amplitudes of aerodynamic load at the first four orders. The former leads to the result that the amplitude at different harmonic numbers converts by means of changing the induced velocity. The latter brings on that the amplitude at each harmonic number alters almost in the same direction, and then leads to an approximate shift of curve, as shown in Fig. 22(b).

The valley loads at the advancing side during the low-velocity circling flight drop with the decrease of circling radius, which is accompanied with high-frequency vibrations. Owing to the apparent decrease of the first-order aerodynamic loads, the flap bending moment at the high-velocity circling state presents a translation at different circling radii. Besides, the valley phase of the flap bending moment has a significant backward shift in the high-velocity flight.

The wake, aerodynamic loads, and structural loads at $R_{\text{cir}} = 400$ m are depicted in Fig. 23, where Fig. 23(a) shows the wake distribution at different circling velocities, Figs. 23(b) and (c) are the distributions of aerodynamic and structural loads along the azimuth, and Figs. 23(d) and (e) present the amplitude of aerodynamic and structural loads at different

harmonic numbers during the variation of circling radius. The velocity affects the density of rotor wakes, whose influence is weakened with the increase of circling velocity. The manipulation value begins to replace the wake distortion, and becomes a dominant factor which affects the distributions of aerodynamic loads. As shown in Figs. 23(b)-(e), the peaks of loads appear in states of small and large circling radius, which are smaller than the extreme position in the middle flight velocity. Because the inertial force is positively correlated to the circling velocity, the flap bending moment changes obviously and the conclusions are different with the variation of circling radius.

4.4. Analysis of flight parameters

Sample flight states selected at intervals along circling velocity and radius are calculated for the sake of a comprehensive analysis regarding the circling flight. The Radial Basis Function (RBF) interpolation method in the following is employed:

$$\begin{cases} \Phi(x, y) = \exp \left(-\frac{(x-x_i)^2}{2\sigma_x^2} - \frac{(y-y_j)^2}{2\sigma_y^2} \right) \\ z(x, y) = \sum w_{ij} \Phi(x, y) \end{cases} \quad (27)$$

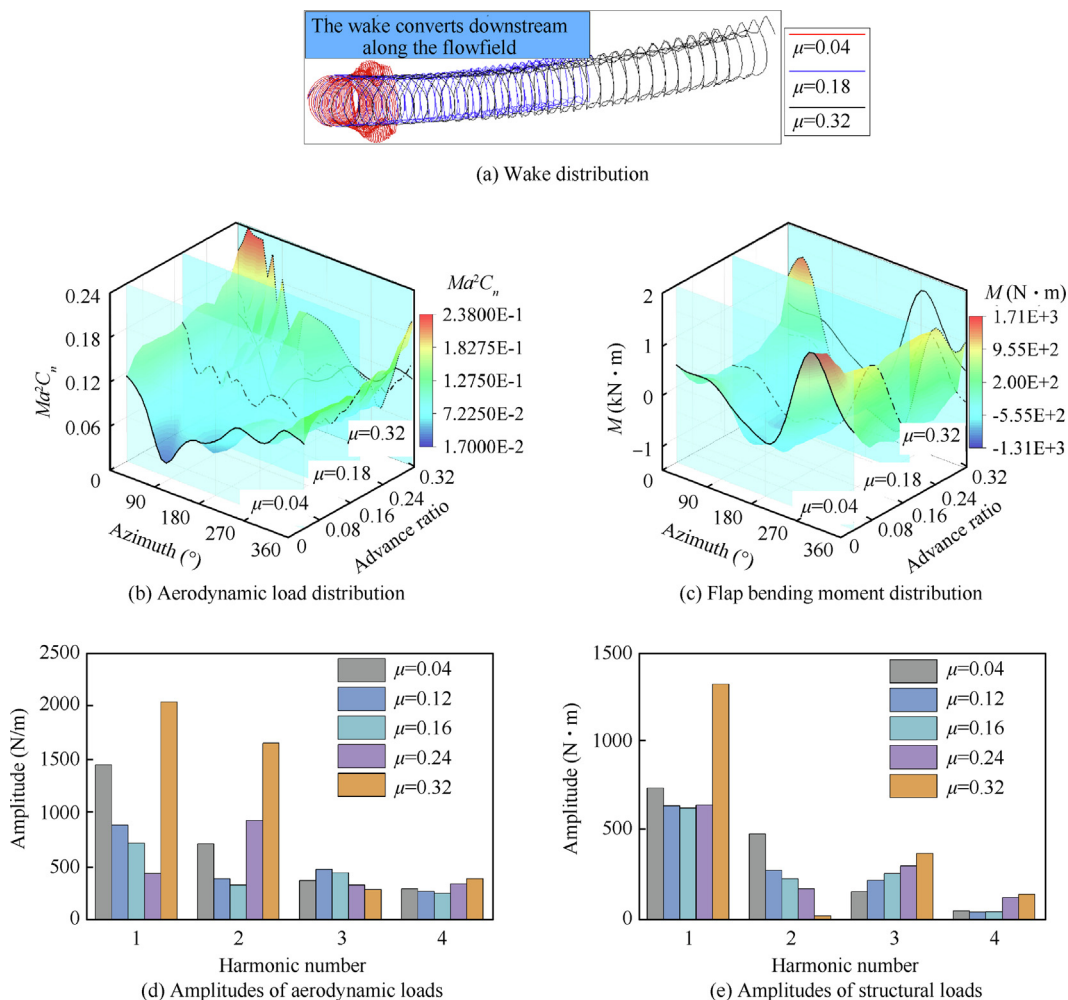


Fig. 23 Wakes, aerodynamic loads, and structural loads around circling velocity at $R_{\text{cir}} = 400$ m.

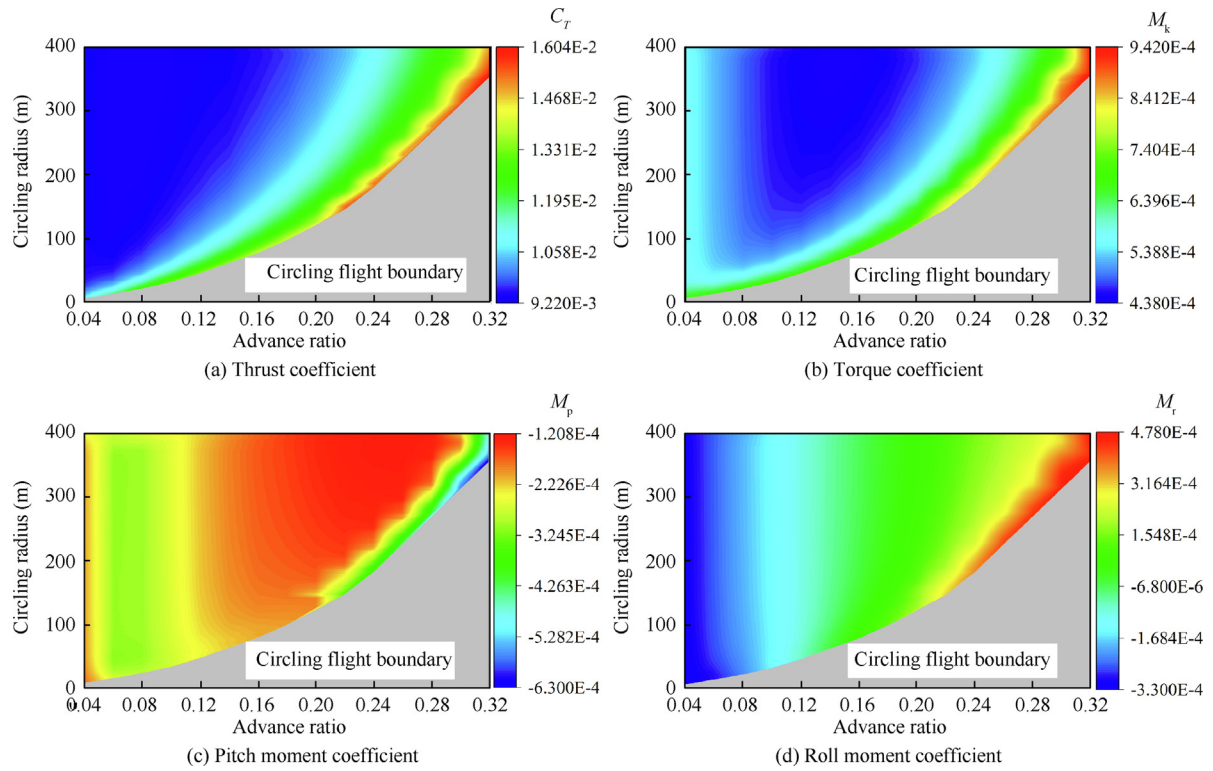


Fig. 24 Distribution of forces and moments of main rotor.

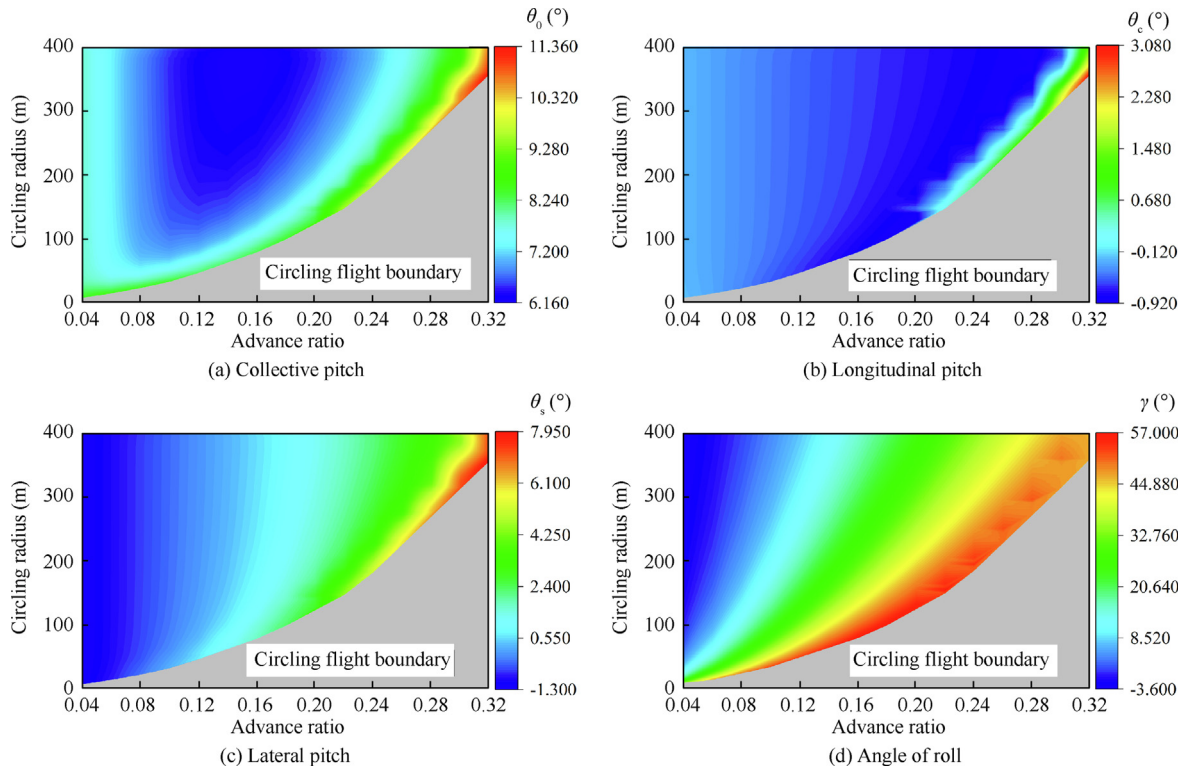


Fig. 25 Distribution of manipulation value.

where (x_i, y_j) are the input values of samples, including the advance ratio μ and the circling radius R_{cir} ; (x, y) are the uncertain input state values, w_{ij} is the weight of each RBF and z is the output value regarding the coefficients of thrust, torque, pitch moment and roll moment (C_T , M_k , M_p , and M_r respectively); σ_x and σ_y are the widths of the RBF in the x and y directions, respectively.

Fig. 24 shows the coefficients of thrust, torque, pitch moment and roll moment considering different flight parameters, and **Fig. 25** gives the manipulation value and attitude angle. The force and moment coefficients fluctuate with flight parameters, and the distribution of thrust and torque coefficients versus the circling radius and velocity forms a valley region. The thrust forms a saddle-shaped curve on account of the trim condition in the forward flight, where the thrust coefficients at low speed and high speed have almost identical torque distributions. The pitch and roll moments are almost unaffected by the circling flight except at the limited radius region of high velocities. The pitch moment deciding the inclination of helicopter increases with the change of longitudinal periodic pitch. The roll moment deciding the roll of helicopter increases with the change of lateral periodic pitch. As far as each velocity is concerned, the two moments and roll angle reach the peak in the region near the circling flight boundary.

According to the analysis above, it is obvious that the distortion of wake has a significant effect on the aerodynamic and structural loads near the circling boundary at low flight veloc-

ities. **Fig. 26** and **Fig. 27** depict the distributions of aerodynamic and structural loads in the rotor disc for $\mu = 0.04$ and the corresponding circling radii. There is a pair of adjacent peak and valley regions in the advancing side of rotor at $R_{\text{cir}} = 8$ m, showing the existence of second interference between the blades and vortices. With the increment of the circling radius, the valley region moves inwards along the blade and towards the positive direction of azimuth angle, while the peak region presents an opposite moving direction. This aerodynamic interference phenomenon can be described as the ‘rotating dipole’, and its intensity decreases apparently in the low-velocity circling flight. The peak and valley regions shift along the circumferential direction in the result of structural load.

As demonstrated by **Fig. 12(a)**, although the vortexes have converted downstream in Zone B-1, they are affected by the circling and accumulated in the advancing side of rotor. Actually, the original vortexes are located above the rotor disc due to the huge rolling angle at the moment. The vector direction of vortex segment is different from the newly-formed vortex and the blade/vortex interaction is formed in an opposite direction. The position of this interference moves towards the negative direction of azimuth angle with the increase of circling radius, and the trends of peak and valley regions are consistent with the degree of wake distortion. As a result, the structural responses of blades also change under the excited aerodynamic loads.

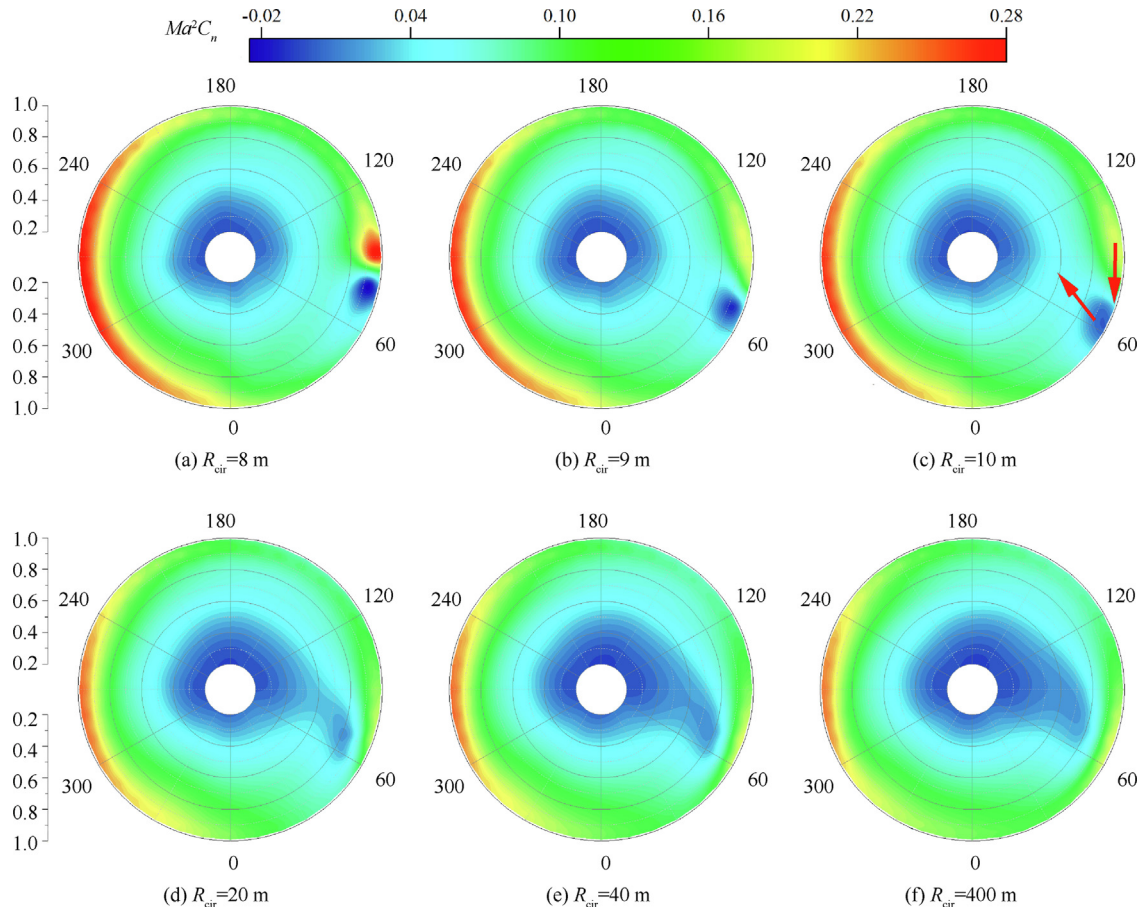


Fig. 26 Distribution of aerodynamic load in rotor disc at $\mu = 0.04$.

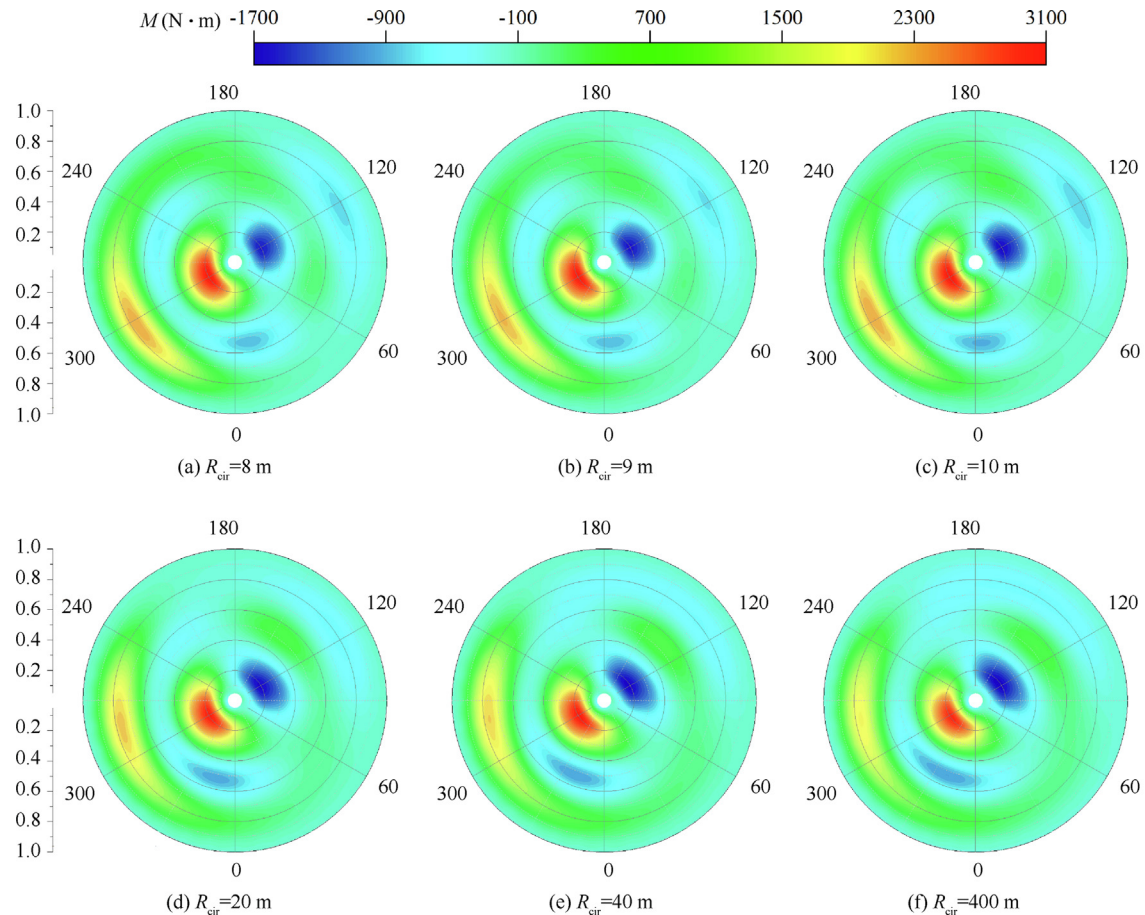


Fig. 27 Distribution of bending moment in rotor disc at $\mu = 0.04$.

5. Conclusions

This study develops a method to simulate the flowfield of the rotor wake during circling flight, and the modal superposition method is introduced to solve the structural responses. The accuracy of the methods are validated by comparisons with the test data of UH-60A. By means of parametric analyses, the conclusions are summarized as follows:

- (1) Circling parameters make great difference to the generation and evolution of vortices, and change the induced velocities of the rotor disk directly. Among these parameters, the circling radius only has a significant influence on the region where the helicopter has the maximum inertia force and the wake distorts severely. The circling direction and velocity have great effect on the aerodynamic loads, i.e., the distributions of the harmonic excitations are changed.
- (2) The circling direction plays an important role in the performance of aerodynamic and structural loads. Leftward circling enhances the origin periodicity of the aerodynamic and structural loads, while the amplitudes of several dominant modes decline in the rightward circling condition.
- (3) When the influence of circling radius becomes stronger, the distortion of vortex will affect the distributions of the induced velocity and the aerodynamic loads, leading

to the apparent rise of flap bending moment in the rightward circling condition. The increase of circling velocity causes the growth of wake speed and decreases the influence of wake on aerodynamic loads, and at this moment the manipulation becomes the main factor of the increasing vibration.

- (4) The distortion of wake leads to the blade/vortex interaction when the helicopter circles at low velocity, in which the advancing side of blade experiences second interference with the motion of vortices. As a result, a pair of peak and valley regions is formed at the blade tip, and causes high-order shocks of aerodynamic loads.

Declaration of Competing Interest

The authors declare that they have no known competing financial interests or personal relationships that could have appeared to influence the work reported in this paper.

Acknowledgments

This work was supported by the National Natural Science Foundation of China (Nos. 12102186, 12032012), the Natural Science Foundation of Jiangsu Province, China (No. BK20200433), the Laboratory Foundation of China (No. 61422202201), the Young Elite Scientists Sponsorship

Program by CAST, China (No. 2022QNRC001), and the Priority Academic Program Development of Jiangsu Higher Education Institutions, China.

References

- Baskett BJ. Aeronautical design standard performance specification handling qualities requirements for military rotorcraft. *AMCOM*. 2000.
- Yang C, Aoyama T. Numerical analysis of maneuvering rotorcraft using moving overlapped grid method. *Trans Japan Soc Aero S Sci* 2008;51(173):151–63.
- Braukmann JN, Wolf CC, Goerttler A, et al. Blade tip vortex system of a rotor with cyclic pitch. *AIAA J* 2020;58(7):2869–80.
- Huang JZ, Peters D. Real-time solution of nonlinear potential flow equations for lifting rotors. *Chin J Aeronaut* 2017;30(3):871–80.
- Hodges DH, Dowell EH. Nonlinear equations of motion for the elastic bending and torsion of twisted nonuniform rotor blades. Washington, D.C.: NASA; 1975. Report No.: NASA-TN D-7818.
- Houbolt JC, Brooks GW. Differential equations of motion for combined flapwise bending, chordwise bending, and torsion of twisted nonuniform rotor blades. Washington, D.C.: NASA; 1957. Report No.: NACA-TN-3905.
- Ferhatoglu E, Cigeroglu E, Özgüven HN. A new modal superposition method for nonlinear vibration analysis of structures using hybrid mode shapes. *Mech Syst Signal Process* 2018;107:317–42.
- Ma YH, Wang YF, Wang C, et al. Interval analysis of rotor dynamic response based on Chebyshev polynomials. *Chin J Aeronaut* 2020;33(9):2342–56.
- Ickes J, Wang JY, Zhao QY, et al. Coupled CFD/CSD simulations of helicopter rotors with a free wake model. *Proceedings of the 52nd aerospace sciences meeting*; National Harbor, Maryland. Reston: AIAA; 2014.
- You Y, Na D, Jung SN. Improved rotor aeromechanics predictions using a fluid structure interaction approach. *Aerospace Sci Technol* 2018;73:118–28.
- Kim JW, Park SH, Yu YH. Euler and Navier-Stokes simulations of helicopter rotor blade in forward flight using an overlapped grid solver. *19th AIAA computational fluid dynamics*; San Antonio, Texas. Reston: AIAA; 2009.
- Ma L, Zhao QJ, Zhang K, et al. Aeroelastic analysis and structural parametric design of composite rotor blade. *Chin J Aeronaut* 2021;34(1):336–49.
- Zhang XY, Wang HL, Zhao QJ, et al. Structural modeling and dynamic analysis of the two-segment deployable beam system. *Int J Mech Sci* 2022;233:107633.
- Ilie M. A fully-coupled CFD/CSD computational approach for aeroelastic studies of helicopter blade-vortex interaction. *Appl Math Comput* 2019;347:122–42.
- Abhishek. Prediction of helicopter blade load for an unsteady pull-up maneuver using lifting-line and CFD/CSD analyses. *J Aerospace Sci Technol* 2013;65(2):178–95.
- Sebastian T, Shreyas A, James DB. Wake-coupling CFD-CSD analysis of helicopter rotors in steady and maneuvering flight conditions. *AHS specialists conference*; San Francisco, California, USA. Fairfax: AHS International, Inc; 2010. p. 758–77.
- Jr Jeffrey DK, Mckillip RM, Wachspress DA, et al. A free wake linear inflow model extraction procedure for rotorcraft analysis. *73rd annual AHS international forum and technology display*; 2017 May 9–11; Fort Worth, Texas, USA. Fairfax: AHS International, Inc; 2017. p. 1972–89.
- Rand O, Khromov V. Free-wake-based dynamic inflow model for hover, forward, and maneuvering flight. *J Am Helicopter Soc* 2017;63(1):012008.1–012008.16.
- Hu MY, Wang AW, Zhang XM. Approximate analytical solutions and experimental analysis for transient response of constrained damping cantilever beam. *Appl Math Mech -Engl Ed* 2010;31(11):1359–70.
- Storch J, Elishakoff I. Vibration of functionally graded rotating beams including the effects of nonlocal elasticity. *AIAA J* 2016;55(4):1480–6.
- Dong SP, Li L, Zhang DG. Vibration analysis of rotating functionally graded tapered beams with hollow circular cross-section. *Aerospace Sci Technol* 2019;95:105476.
- Sun QZ, Xing YF, Liu B, et al. Accurate closed-form eigensolutions of three-dimensional panel flutter with arbitrary homogeneous boundary conditions. *Chin J Aeronaut* 2023;36(1):266–89.
- Beddoes TS. Representation of airfoil behavior. *Vertica* 1983;7(2):183–97.